Predicting the variance of ML reconstructions with body contour constraint for multi-pinhole SPECT

Lin Zhou, Kathleen Vunckx and Johan Nuyts

***Abstract*— A well known limitation of the multi-pinhole system is that the reconstructed images may suffer from artifacts due to truncated and/or overlapping projections. A previous study showed that these artifacts can be strongly suppressed by using prior knowledge about the object boundary, which is typically obtained from a CT- or MRI-scan acquired in the same pose. Forcing the reconstructed activity outside the object contour to zero effectively eliminated the artifacts. In this study, we investigate the validity of an analytical image quality prediction method, which previously has been used to optimize the multi-pinhole system, with and without the application of body contour constraint in the post-smoothed MLEM reconstruction.**

The results indicate that the use of the body contour constraint has hardly noticeable effects on the variance, which is well predicted by the analytical method. In contrast, the contour constraint eliminated the bias and artifacts as expected. The analytical method assumes an unbiased estimator, and therefore, it is a good predictor for post-smoothed MLEM with body contour constraint. Because the information about the body contour is often available in small animal imaging, we conclude that it seems valid to use the analytical method for optimizing the design of multi-pinhole collimators.

I. Introduction

Designing multi-pinhole collimators is a challenging task because of the large amount of parameters that are involved: the number of pinhole apertures, their positions relative to the detector and to each other, the diameter, orientation and acceptance angle of each aperture. To implement an efficient and possibly semi-automated optimization, one needs a fast and reliable way to compute figures of merit. We have previously proposed to use the analytical approach of [1], [2] to predict the variance on the reconstructed pixel value (or on the mean over a region of interest (ROI), or on the channelized Hotelling Observer (CHO) statistic) to assess the performance of a particular tomographic system for imaging a particular tracer distribution at a pre-defined spatial resolution [3]–[7].

One limitation of the multi-pinhole system is that the reconstructed images may suffer from artifacts due to truncated and/or overlapping projections [7]–[10]. For example, as shown in Fig. 1 (left), if the sensitivities of the two pinholes overlap, the projection value acquired through one pinhole may be back-projected through the other pinhole during the reconstruction, leading to the assignment of positive values to the background where the true activity is zero. As the camera and the pinhole collimator rotate around the object, this yields ring-pattern artifacts in the background. However, if the background is known in some way before or during the reconstruction, the ring artifact can be strongly suppressed or eliminated. One way to achieve this goal is to use prior knowledge about the body contour of the object (Fig. 1, right), which typically can be obtained from a CT- or MRI-scan acquired in the same pose. In [11], [12], it is shown that forcing the reconstructed activity outside the object contour to zero can effectively eliminate the artifacts.

In this study we investigate the validity of the analytical method for predicting the variance of post-smoothed MLEM reconstructions with and without the application of body contour constraint.

Dept. of Nuclear Medicine, K.U.Leuven, B-3000 Leuven, Belgium.

This work is supported by F.W.O. grant G.0569.08., I.U.A.P. grant NIMI and 2010 IEEE NSS-MIC trainee grant.

II. Method

A. Analytical Method

By computing an approximated pseudo-inverse of the Fisher information matrix, the spatial resolution and covariance matrix of the reconstructed pixel values can be estimated analytically [1], [2]. We have used this approach to compare different tomographic systems for the task of imaging the same tracer distribution at a predefined spatial resolution [3]–[7]. The different systems apply post-filtered maximum likelihood reconstruction to yield images with the same spatial resolution. The system that can do this with the lowest variance (on pixel values, ROI values, CHO statistic, ...) is then considered as the best system.

For a certain pixel j in the reconstruction image Λ, we define a set of filters:

$$Q_L^j = P^j G^j F^j \tag{1}$$

$$Q_C^j = P^j G^j F^j G^{jT} P^j \tag{2}$$

All the matrices are in $\mathbb{R}^{N\times N}$, with N the total number of voxels in the image space. F^j is the approximated Fisher information matrix, G^j is the approximate pseudoinverse of F^j, P^j is an isotropic Gaussian post-smooth filter that tries to impose the given target resolution, ^{T} denotes transpose. All factors are j-dependent due to the assumption of local shift-invariance. For details on the implementation, see [6].

For the chosen pixel j, the contrast recovery coefficient (CRC) and the variance (VAR) can be approximated as:

$$\text{CRC}^j \approx e^{jT} Q_L^j e^j \tag{3}$$

$$\text{VAR}^j = (\sigma^j)^2 \approx e^{jT} Q_C^j e^j \tag{4}$$

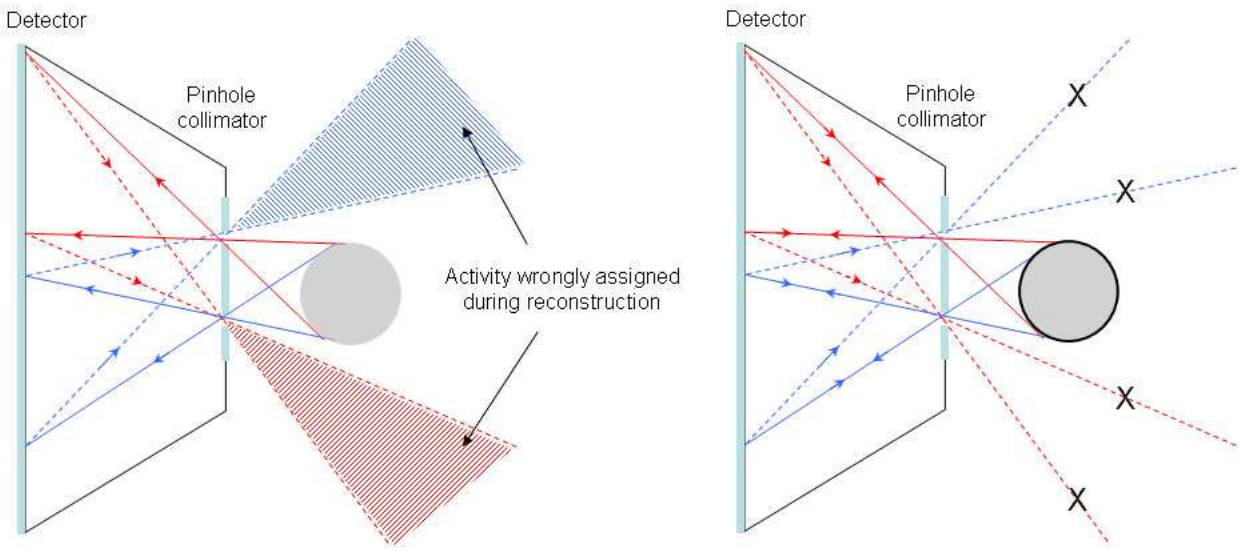

Fig. 1. Multi-pinhole projection and back-projection. Left: without body contour constraint, Right: with body contour constraint.

with e^j the j-th unit vector. The contrast-to-noise ratio (CNR) of pixel j is calculated as:

$$\text{CNR}^j = \text{CRC}^j / \sqrt{\text{VAR}^j} = \text{CRC}/\sigma^j \tag{5}$$

Since we impose the same target resolution, CRC is constant. Thus it is equivalent to using the standard deviation σ^j to evaluate the relative performance of different pinhole systems.

B. Numerical Simulations

To estimate the overall image quality, including the effect of the artifact in the reconstruction image, we added Poisson noise to the sinogram and then performed post-smoothed MLEM reconstructions. The reconstruction was done for two cases: without/with the prior knowledge of the body contour. In the latter case, an image which has non-zero voxel values within the phantom contour and zero elsewhere, was used as the initial image for the reconstruction. Because the MLEM algorithm is multiplicative, this initialization guarantees that the background will remain zero in the subsequent iterations. In both cases, we calculated the root mean squared deviation (RMSD) between the final reconstruction image and the original phantom:

$$\text{RMSD} = \sqrt{\frac{1}{I}\sum_{j\in\text{VOI}} (\text{recon}^{ps}[j] - \text{phantom}^{ps}[j])^2} \tag{6}$$

where j is the index of the voxel in the image space, VOI is the volume of interest (in this study it is the volume inside the object contour), I is the total number of voxels in the VOI, and the superscript ^{ps} indicates that the image (or the reconstruction) is smoothed to the target resolution. Note that Eq. (6) combines both the noise and the bias.

C. Validation of Analytical Method

To estimate the accuracy of σ^j in II-A, its value can be verified by numerical simulations using multiple noise realizations:

$$\sigma^j = \sqrt{\frac{1}{M-1}\sum_{m=1}^{M}\left(\text{recon}_m^{ps}[j] - \frac{1}{M}\sum_{m=1}^{M}\text{recon}_m^{ps}[j]\right)^2} \tag{7}$$

where the subscript m represents the m-th noise realization, and M is the total number of noise realizations. Similar as in II-B, the validation was also performed for both cases.

III. Simulation

The study was performed with both two-dimensional (2-D) and three-dimensional (3-D) pinhole systems, shown in Fig. 3 (left) and Fig. 4 (left), respectively. The pinholes were located either on a line (2-D) or a plane (3-D) parallel to the detector. It was assumed that the center of the detector array, the central pinhole and the center of the image space were collinear. The distance between the central pinhole and the detector was 176 mm, and the distance between the central pinhole and the center of the image space was 25 mm. 64 acquisition angles were equally distributed over 360 degrees. The pixel size in detection space and image space was 1.95 mm and 0.6 mm, respectively.

For the 2-D and 3-D pinhole systems, we modeled 5 and 4 different pinhole configurations, respectively. In the 2-D case, the offset of the pinholes (pinoff) with respect to the central pinhole were (a) [0], (b) [-15,0,10], (c) [-15,0,15], (d) [-15,0,20] and (e) [-5,0,5], with unit of mm. The acceptance angle (AA) of all the apertures was 120°. In the 3-D case (see Fig. 2), the settings were (f) 1 pinhole at the center (AA = 120°), (g) 7-pinhole configuration optimized in [7], (h) 1 pinhole at the center and 6 pinholes distributed over two concentric circles (radius = 15 mm and 20 mm, AA = 60°), and (i) 1

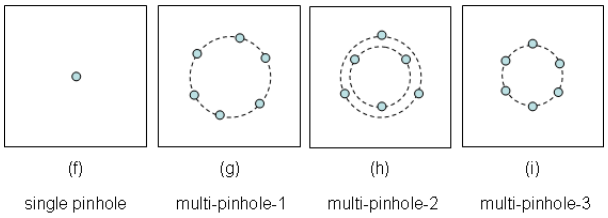

Fig. 2. Four different 3-D pinhole configurations.

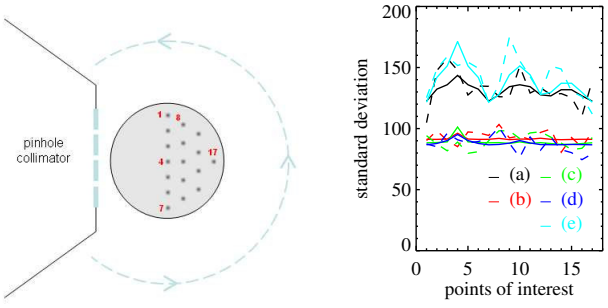

Fig. 3. Left: Disk phantom and points of interest. Right: Validation of analytical method. σ^j calculated from the analytical method and from the numerical simulation are plotted by solid lines and dashed lines, respectively. The simulations were performed with body contour constraint. The 5 different colors represent the 5 different pinhole configurations described in III.

pinhole at the center and 6 pinholes equally spread over one circle (radius = 15 mm, AA = 60°). The diameter of each pinhole was 1.5 mm and the FWHM of the target resolution was 1.8 mm. The position dependent sensitivity of the pinhole systems was modeled in the same way as in [7]. Note that there were different degrees of overlap in the sensitivity with all proposed multi-pinhole configurations.

The phantom parameters and the reconstruction settings used for this study are listed in Table I. The method of II-A was applied to all points of interest shown in Fig. 3 (left) and Fig. 4 (left). Using the analytical method, σ^j of every point was

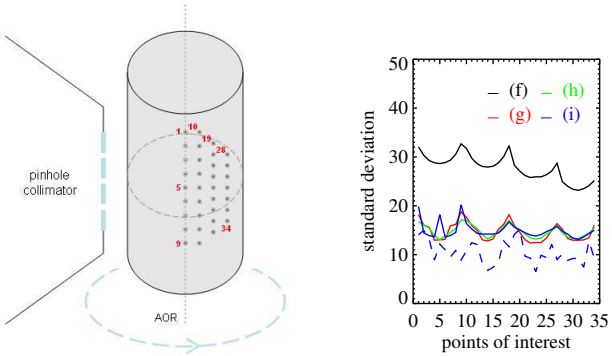

Fig. 4. Left: Cylindric phantom and points of interest. Right: Validation of analytical method. σ^j calculated from the analytical method and from the numerical simulation are plotted by solid lines and a dashed line, respectively. The simulations were performed with body contour constraint. The 4 different colors represent the 4 different pinhole configurations described in III.

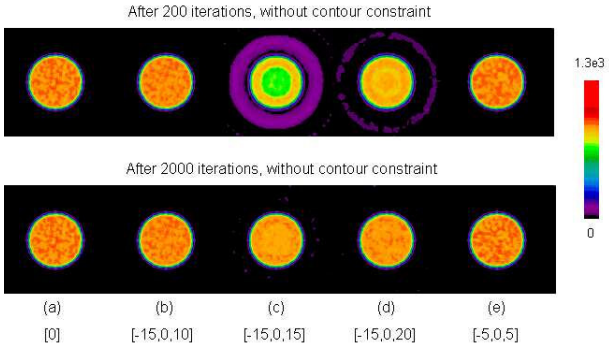

Fig. 5. Post-smoothed 2-D reconstruction images after 200 iterations (top row) and 2000 iterations (bottom row) without the body contour constraint.

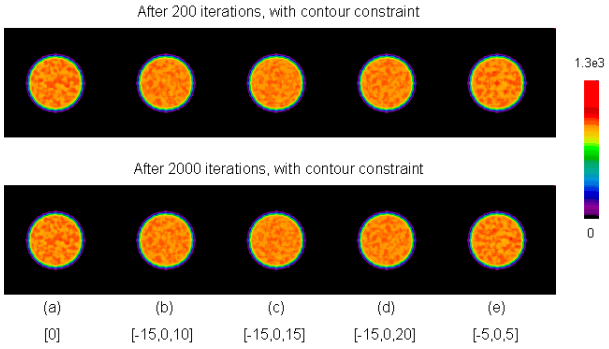

Fig. 6. Post-smoothed 2-D reconstruction images after 200 iterations (top row) and 2000 iterations (bottom row) with the body contour constraint.

calculated and compared to the value obtained from Eq. (7). The validation was done for all 2-D pinhole configurations and the last 3-D pinhole configuration (i), using reconstructions both with and without body contour constraint. Note that for the 2-D pinhole setup, in the case of imposing the body contour, we used a ring-pattern image as the initial image in the reconstruction which encourages the introduction of artifacts. However in the 3-D case a uniform cylinder was used as the initial image considering the slow convergence of 3-D pinhole reconstruction.

IV. Result

The validation results with body contour constraint are shown in Fig. 3 (right) and Fig. 4 (right) for the 2-D pinhole and 3-D pinhole designs, respectively. It can be seen that for the 2-D pinhole case the σ^j yielded from the analytical method are in good agreement with those from the numerical simulations, while for the 3-D pinhole case the σ^j are slightly overestimated by the analytical method.

Figs. 5 and 6 show the reconstruction images for the cases without/with body contour constraint. Fig. 7 plots the RMSD as a function of the number of iterations in both cases. If no body contour constraint is applied, the reconstructions with pinhole configurations (a), (b) and (e) are nearly artifact-free, while with (c) and (d) the reconstructions suffer from obvious ring artifacts which are not completely eliminated even after 2000 iterations.

TABLE I

SIMULATION PARAMETERS

Pinhole setting	2-D pinhole	3-D pinhole
Configuration index	(a), (b), (c), (d), (e)	(f), (g), (h), (i)
Detector array	256x1	256x200
Image dimension	73x73	72x72x88
Phantom activity	1.08×10^4 Bq/pixel	1.08×10^3 Bq/voxel
Phantom type	uniform disk	uniform cylinder
Phantom diameter	21.6 mm	25.2 mm
Initial recon (with body contour)	disk with ring pattern	uniform cylinder
Number of noise realizations	100	20
Number of MLEM iterations	2000	equivalently 1800 (with OSEM)

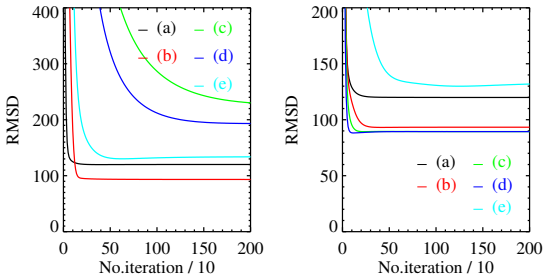

Fig. 7. Plot of RMSD as a function of number of iterations. Left: without body contour constraint. Right: with body contour constraint. The 5 different colors represent the 5 different 2-D pinhole settings.

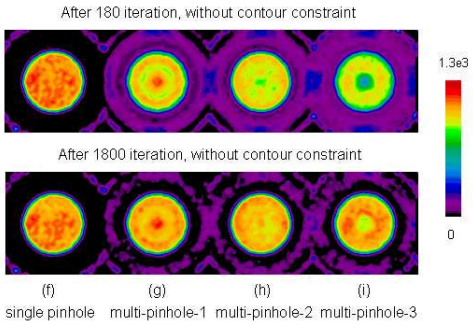

Fig. 8. Central slices of post-smoothed 3-D reconstruction images after 180 iterations (top row) and 1800 iterations (bottom row) without the body contour constraint.

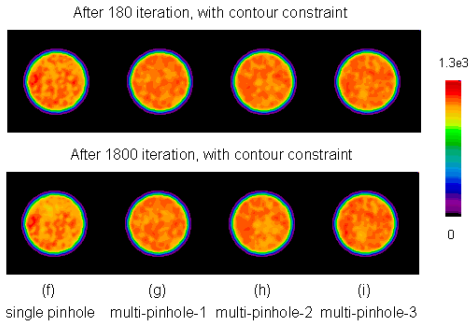

Fig. 9. Central slices of post-smoothed 3-D reconstruction images after 180 iterations (top row) and 1800 iterations (bottom row) with the body contour constraint.

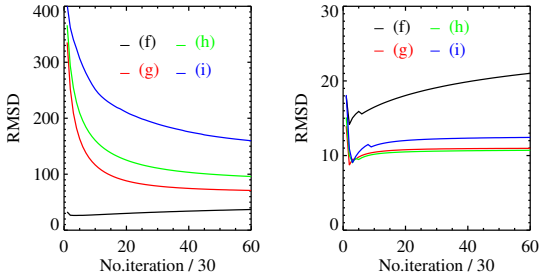

Fig. 10. Plot of RMSD as a function of number of iterations. Left: without body contour constraint. Right: with body contour constraint. The 4 different colors represent the 4 different 3-D pinhole settings.

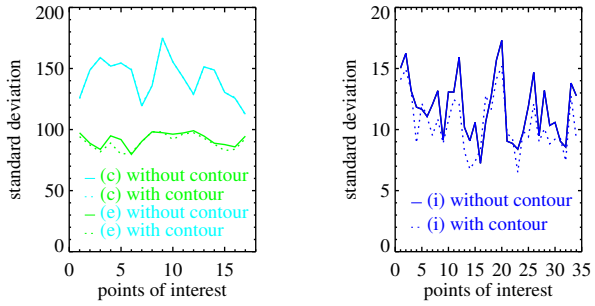

Fig. 11. Standard deviation σ^j from repeated simulations, calculated for each point of interest with 2-D configurations (c) and (e) and 3-D configuration (i). The solid/doted line represents σ^j calculated without/with body contour constraint, respectively.

With the use of exact knowledge about the body contour, the artifact is significantly suppressed. In the latter case, the ranking of system performance based on RMSD corresponds well with that given by the analytical method (Fig. 3), meaning that the bias in the reconstruction is greatly reduced. The corresponding reconstructions and the RMSD values for 3-D pinhole are shown in Fig. 8 - Fig. 10. These figures show that the results obtained with 3-D pinhole are very similar to those from the 2-D pinhole configurations.

Fig. 11 compares σ^j obtained from simulations without/with applying the body contour constraint for pinhole configurations

(c), (e) and (i). The plots show that the application of the constraint has no effect on the variance inside the reconstructed object if there is no background artifact without body contour constraint (e.g. with pinhole setting (e)). However, if the reconstruction originally suffers from ring artifact in the background (e.g. with pinhole settings (c) and (j)), the σ^j with body contour constraint are slightly lower than those without the contour constraint, but the difference is very small.

V. Discussion

There are two determinants of the background artifact with multi-pinhole systems, i.e., the pinhole configuration and the object size. For example, in the 2-D case, the reconstructions with multi-pinhole (b) and (e) do not suffer from the background artifact even though they have overlapped sensitivities. It is because the background is "clearly seen" in at least some of the projection views. In other words, there are some detector pixels with zero count, because the ray(s) corresponding to that pixel do not intersect the object. Such zero count values provide knowledge about the cold background. With multi-pinhole configurations (c) and (d), the background ring artifacts are reduced at high iteration, but the bias due to non-negative noise in the background persists after 2000 iterations. This bias cannot be predicted by Eq. (3) because it assumes an unbiased estimator. The prior information about the body contour strongly suppresses these background artifacts, and at the same time makes the reconstruction nearly bias-free.

VI. Conclusion

Applying MLEM with body contour constraint results in (nearly) bias-free images, the variance of which is well predicted with the analytical method. Because the information about the body contour is often available in small animal imaging, we conclude that it seems valid to use the analytical method for optimizing the design of multi-pinhole collimators.

References

[1] J. A. Fessler and W. L. Rogers, "Spatial resolution properties of penalized likelihood image reconstruction: space-invariant tomographs." *IEEE Trans. Image Proc.*, 5(9), pp. 1346-1358, 1996.

[2] J. Qi and R. M. Leahy, "Resolution and noise properties of MAP reconstruction for fully 3-D PET." *IEEE Trans. Med. Imag.*, 19(5), pp. 493-506, 2000.

[3] K. Vunckx, D. Bequé, M. Defrise and J. Nuyts, "Single and multipinhole collimator design evaluation method for small animal SPECT." *IEEE Trans. Med. Imag.*, 27(1), pp. 36-46, 2008.

[4] L. Zhou, K. Vunckx and J. Nuyts, "Comparison between parallel hole and rotating slat collimation with a contrast phantom using an analytical method", *IEEE Nuclear Science Symposium Conference Record*, pp. 3678-3681, 2009.

[5] L. Zhou, M. Defrise, K. Vunckx and J. Nuyts, "Comparison Between Parallel Hole and Rotating Slat Collimation: Analytical Noise Propagation Models.", *IEEE Trans. Med. Imag.*, in press.

[6] J. Nuyt, K. Vunckx, M. Defrise and C. Vanhove, "Small animal imaging with multi-pinhole SPECT.", *Method*, 48(2), pp. 83-91, 2009.

[7] K. Vunckx, P. Suetens and J. Nuyts, "Effect of overlapping projections on reconstruction image quality in multipinhole SPECT." *IEEE Trans. Med. Imag.*, 27(7), pp. 972-983, 2008.

[8] S. R. Meikle, P. Kench, A. G. Weisenberger, R. Wojcik, M. F. Smith, S. Majewski, S. Eberl, R. R. Fulton, A. B. Rosenfeld and M. J. Fulham, "A prototype coded aperture detector for small animal SPECT.", *IEEE Trans. Nucl. Sci.*, 49(5), pp. 2167-2171, 2002.

[9] L. J. Meng and D. K. Wehe, "Feasibility study of using hybrid collimation for nuclear environmental imaging.", *IEEE Trans. Nucl. Sci.*, 50(4), pp. 1103-1110, 2003.

[10] G. S. P. Mok, Y. C. Wang and B. M. W. Tsui, "Quantification of the Multiplexing Effects in Multi-Pinhole Small Animal SPECT: A Simulation Study.", *IEEE Trans. Nucl. Sci.*, 56(5), pp. 2636-2643, 2009.

[11] K. Vunckx, J. Nuyts, B. Vanbilloen, M. De Saint-Hubert, D. Vanderghinste, D. Rattat, F. M. Mottaghy, and M. Defrise, "Optimized multipinhole design for mouse imaging." *IEEE Trans. Nucl. Sci.*, 56(5), pp. 2696-2705, 2009.

[12] F. P. DiFilippo and S. Patel, "Strategies to reduce artifacts and improve accuracy in multiplexed multi-pinhole small animal SPECT." *IEEE Nuclear Science Symposium Conference Record*, pp. 3151-3154, 2009.